Nanoscale Horizons

COMMUNICATION

View Article Online
View Journal | View Issue

Cite this: *Nanoscale Horiz.*, 2019, **4**, 1434

Received 5th May 2019,
Accepted 16th July 2019

DOI: 10.1039/c9nh00260j

rsc.li/nanoscale-horizons

Growth of 2H stacked WSe_2 bilayers on sapphire†

Ali Han,[a] Areej Aljarb,[a] Sheng Liu,[b] Peng Li,[a] Chun Ma,[a] Fei Xue,[a] Sergei Lopatin,[c] Chih-Wen Yang,[a] Jing-Kai Huang,[ad] Yi Wan,[a] Xixiang Zhang,[a] Qihua Xiong,[efg] Kuo-Wei Huang,[a] Vincent Tung,*[ah] Thomas D. Anthopoulos*[a] and Lain-Jong Li*[ad]

Bilayers of two-dimensional (2D) transition metal chalcogenides (TMDs) such as WSe_2 have been attracting increasing attention owing to the intriguing properties involved in the different stacking configurations. The growth of bilayer WSe_2 by chemical vapor deposition (CVD) has been facilely obtained without proper control of the stacking configuration. Herein, we report the controlled growth of bilayer WSe_2 crystals as large as 30 μm on *c*-plane sapphire by the CVD method. Combining second harmonic generation (SHG), low-frequency Raman and scanning transmission electron microscopy (STEM), we elucidate the as-grown bilayer WSe_2 with a 2H stacking configuration. Atomic force microscope (AFM) measurements reveal that the prominent atomic steps provide the energetically favorable templates to guide the upper layer nuclei formation, resembling the "graphoepitaxial effect" and facilitating the second WSe_2 layer following the layer-by-layer growth mode to complete the bilayer growth. Field-effect charge transport measurement performed on bilayer WSe_2 yields a hole mobility of up to 40 $cm^2 V^{-1} s^{-1}$, more than 3× higher than the value achieved in monolayer WSe_2-based devices. Our study provides key insights into the growth mechanism of bilayer WSe_2 crystals on sapphire and unlocks the opportunity for potential bilayer and multilayer TMD electronic applications.

New concepts

Transition metal dichalcogenide van der Waals thin layers like WSe_2 are considered promising for extending Moore's law for future electronics. However, a monolayer exhibits lower mobility due to serious charge impurity scattering at interfaces. Bilayers have better chance to serve for future electronics owing to superior charge screening. However, a controllable method to grow large-area bilayer WSe_2 is yet to be developed. In this manuscript, we synthesize highly crystalline bilayers WSe_2 with a pure 2H stacked configuration on *c*-plane sapphires by a CVD method and unravel the growth mechanism. The WSe_2 bilayers crystals were controllably grown with a pure 2H stacking configuration. Fundamentally, the formation of nuclei is found to follow the "graphoepitaxy mechanism" but the stacking follows the epitaxial growth mechanism. With the proposed growth method, large-area pure bilayer WSe_2 can be obtained. These observations shed light on the control of the large-area growth of bilayers for electronics applications. Practically, we proved that the field-effect mobility extrapolated from the CVD bilayer WSe_2 based FET devices yields a hole mobility of up to 40 $cm^2 V^{-1} s^{-1}$, rivalling that of monolayer WSe_2 crystals grown from CVD methods.

Semiconducting TMD layer materials with the formula of MX_2 (M = Mo, W; X = S, Se) have been considered as promising candidates to extend Moore's Law[1] for next-generation electronics, optoelectronics and valleytronics.[2–6] Like many other 2D material systems, the electronic properties of TMDs strongly depend on the number of layers and the stacking configurations. Until now, researchers have developed two mainstream approaches to synthesize monolayer or multilayer TMDs: top-down strategies of mechanical exfoliation (ME)[5,7] and liquid exfoliation;[8] and bottom-up strategies of CVD,[2–4,9] physical vapor deposition (PVD)[10–12] and molecular beam epitaxy (MBE).[13,14] Due to the low productivity and heavy contamination of few-layer TMDs by top-down approaches, the bottom-up strategies, especially CVD, are quickly becoming the methods of choice as they are capable of controllably producing few layered TMD specimens

[a] *Physical Sciences and Engineering Division (PSE), King Abdullah University of Science and Technology, Thuwal 23955-6900, Kingdom of Saudi Arabia. E-mail: thomas.anthopoulos@kaust.edu.sa, vincent.tung@kaust.edu.sa, lance.li@kaust.edu.sa*
[b] *Division of Physics and Applied Physics, School of Physical and Mathematical Sciences, Nanyang Technological University, 637371, Singapore*
[c] *King Abdullah University of Science and Technology (KAUST), Core Labs, Thuwal, 23955-6900, Kingdom of Saudi Arabia*
[d] *School of Materials Science and Engineering, University of New South Wales, Sydney, NSW 2052, Australia*
[e] *Division of Physics and Applied Physics, School of Physical and Mathematical Sciences, Nanyang Technological University, 637371, Singapore*
[f] *MajuLab, CNRS-UNS-NUS-NTU International Joint Research Unit, UMI 3654, 639798, Singapore*
[g] *NOVITAS, Nanoelectronics Center of Excellence, School of Electrical and Electronic Engineering, Nanyang Technological University, 639798, Singapore*
[h] *Molecular Foundry Division, Lawrence Berkeley National Lab, Berkeley 94720, USA*
† Electronic supplementary information (ESI) available. See DOI: 10.1039/c9nh00260j

through manipulating the electronic interfaces with various stacking configurations.

Specifically, WSe_2 has emerged as the most investigated TMD due to its intrinsic p-type nature that complements the n-type chalcogenide family for a fully integrated circuit design. Thus, the needs for large-size and high-quality monolayer WSe_2 specimens continue to fuel the momentum. Meanwhile, recent experimental observations demonstrated intriguing and unprecedented characters in bilayer WSe_2 stemmed from the spin-valley polarization mediated by stacking configurations[15,16] and the substantial difference in electronic and optical properties between the interlayer reactions. This combination of unique characteristics holds tantalizing prospects for diverse applications, such as valley physics and optoelectronics,[7,17–19] that cannot be realized in monolayer and bulk counterparts. To date, a wide array of approaches have been reported to synthesize high yield monolayer or a few layer WSe_2 by CVD,[9,20–23] however, the study of controllable growth of bilayer WSe_2 with well-defined stacking configurations in conjunction with the growth mechanism is still in its infancy.

Recently, uniform bilayer/trilayer MoS_2 crystals on a SiO_2 substrate have been synthesized by the CVD method;[24,25] however, the growth mechanism and stacking configuration for the bilayers were not investigated. Another report has recognized that the MoS_2 bilayers are usually in the mixed 2H and 3R stacking configurations.[26] Recently, Ye *et al.* reported a mechanistic understanding of vertical growth of TMDs on SiO_2 substrates *via* multiscale modelling to validate experimental observations.[27] Due to the thermal stability and low-cost of SiO_2 substrates, they have been widely used as the growth substrate in most TMDs. Unfortunately, the use of a SiO_2 substrate has many drawbacks, including the amorphous surface microstructure and relatively high surface roughness. As a result, the mobility properties of these TMDs supported on a SiO_2 substrate are limited due to the trapped charges in the interface between TMDs and SiO_2.[28] To this end, systematic investigation of the growth mechanism of bilayer TMDs on an atomically smooth crystalline substrate could potentially help to control the growth for the much-needed controlled manufacturing.

Compared to SiO_2 substrates, commercial *c*-plane sapphire wafers are well-known to develop atomic step-terrace structures on the surface upon high temperature annealing beyond 1000 °C.[22,29,30] It was previously shown that such atomic steps significantly affected the growth of various materials including single wall carbon nanotubes (SWNT),[31,32] GaN nanowires[33] and graphene.[34] For example, the atomic steps-guided formation of SWNTs was proposed to be due to a "wake growth" mechanism, in which the catalyst nanoparticle slides along the atomic steps leaving the growing SWNT behind as a wake. Moreover, the density of atomic steps was shown to profoundly impact on the density and alignment of SWNTs.[32] In the case of GaN nanowires, the guided growth along the atomic steps and grooves was determined by the epitaxial relationship with the substrate and the graphoepitaxial effect.[33] Similarly, the role of atomic step sites for graphene growth on Ni was predicted and explained by Bengaard *et al.*[35] Their calculations revealed that the step-mediated growth occurred because carbon atoms bond stronger to the atomic step sites than to the facets. Moreover, it is energetically favorable for carbon atoms resided at a preferred adsorption site, *e.g.*, steps, to stitch into a graphene layer. More recently, the large area and aligned growth of monolayer MoS_2 and WSe_2 guided by the presence of atomic steps on the sapphire substrate have been reported.[22,30] These results demonstrate that atomic steps on the substrate surface intensively impact the aligned growth for a wide range of low-dimensional materials in both lateral and vertical directions. Despite these pioneering investigations, scalable production of bilayer WSe_2 crystals with controllable stacking configurations is still limited due to the lack of detailed knowledge of the growth mechanism on sapphire.

It has recently been demonstrated that the most stable stacking pattern is 2H among the five-high-symmetry stacking configurations in bilayer TMDs.[36,37] In this work, highly pure 2H stacked bilayer WSe_2 crystals were synthesized on *c*-plane sapphire by CVD and the bilayer WSe_2 growth mechanism was revealed through the using of complementary characterization techniques. 2H stacked bilayer WSe_2 crystals were prepared through a one-step CVD growth process in a tube furnace with selenium (Se) and tungsten trioxide (WO_3) as the precursors[38] (see the method section). Fig. S1 (ESI†) illustrates the CVD setup that we use in the study. Briefly, a quartz tube (inner tube) with a sapphire substrate was inserted into a larger quartz tube. WO_3 and Se were put in the heating zone and in the upstream cold zone, respectively. This dual-tube configuration has been proven to be beneficial for the reactant species concentration accumulation and as a result, WSe_2 nucleation.[38] In Fig. 1a, the optical micrograph image reveals the formation of monolayer and bilayer WSe_2 as large as 30 μm with the optimized experimental parameters. The amount of Se is gradually increased for the growth of large WSe_2 bilayers with the fixed WO_3 precursor loading amount of 0.3 g.

When the amount of Se is ≤ 3 g, scattered WO_{3-x} nanowires or particles are formed (Fig. S2a–c, ESI†). It's been experimentally demonstrated that, for small amounts of Se, almost no WSe_2 ultrathin crystals are formed from the WO_{3-x} nanowires/particles because of the extremely inadequate selenization. On increasing the level of Se loading, the selenization becomes sufficient, and more and more WO_{3-x} is converted into WSe_2.[38,39] When the amount of Se reaches 4 g, the WSe_2 domains are mainly monolayers. When the amount of Se is around 5 g, under the action of a suitable amount of second layer nucleation on the first WSe_2 layer, they continue to grow and cover the first monolayers to form bilayer WSe_2 crystals (layer-by-layer growth). Meanwhile, the WSe_2 domains are scattered across the sapphire substrate with low nucleation density which can permit the large crystal domain size (few tens of micron), as shown in Fig. S2e and f (ESI†).[25,26] When the amount of Se is >5 g, too much WSe_2 nucleation will hamper the enlarging of the WSe_2 monolayer and thus the bilayer dimension (flake size is smaller than 10 μm as shown in Fig. S3, ESI†). The details of the bilayer growth mechanism have been discussed hereafter in this work.

The Raman spectra E^1_{2g} and photoluminescence spectroscopy (PL) of WSe_2 shown in Fig. 1b and c were obtained using

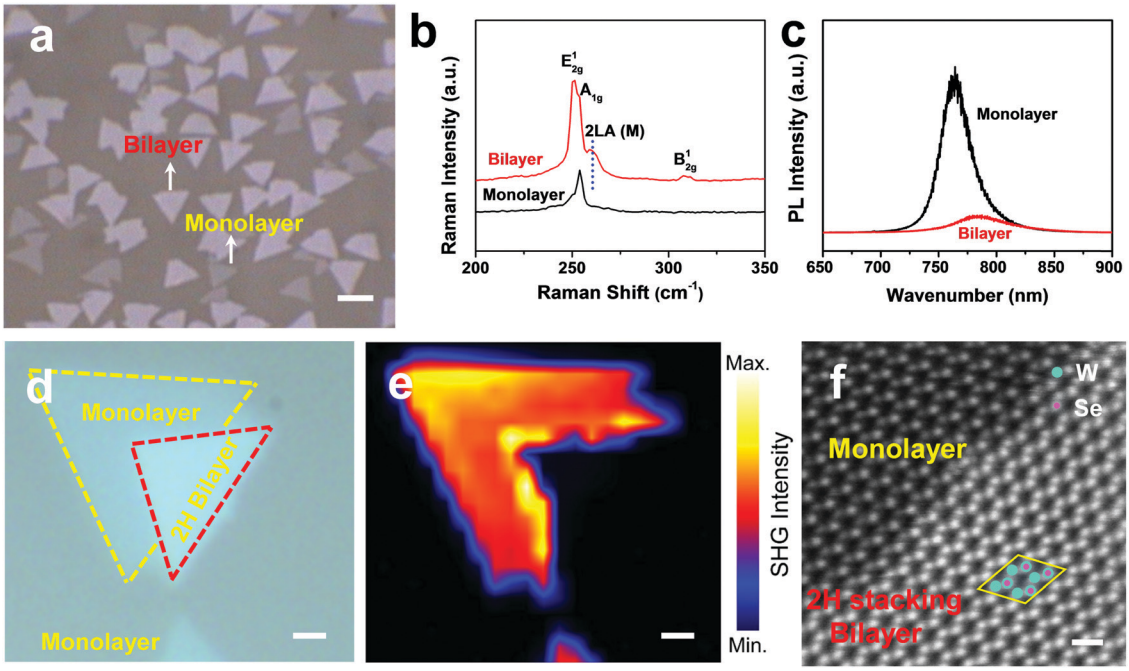

Fig. 1 (a) Optical micrograph of monolayer/bilayer WSe_2 crystals as-grown on a *c*-plane sapphire substrate. The amount of WO_3 is 0.3 g, while the amount of Se powder is 5.0 g. A high purity of H_2/Ar is the carrier gas with a fixed flow rate of 5/65 sccm/sccm. The T_{Se} and T_{WO_3} are maintained at 250 °C and 895 °C, respectively. The growth pressure of the furnace is 10 Torr for the whole CVD growth and the growth time is 15 min; (b) the Raman spectra measurements for monolayer (black) and bilayer (red) WSe_2 crystals; (c) the PL spectra measurements for monolayer (black) and bilayer (red) WSe_2 crystals; (d) optical micrograph of a bilayer WSe_2 crystal with a monolayer WSe_2 crystal as a reference; (e) the corresponding SHG intensity mapping obtained by pixel-to-pixel spatial scanning on the crystals in (d); (f) the HAADF-STEM image for the 2H stacking bilayer WSe_2 crystal (selected from (a)). Scale bars: a, 30 μm; d, 2 μm; e, 2 μm; f, 0.5 nm.

a 532 nm laser as the excitation wavelength. The Raman spectra exhibit the characteristic WSe_2 in-plane vibrational (E^1_{2g}) mode assigned at 251.1 cm^{-1}. The most prominent resonance feature in the case of bilayer WSe_2 as compared with monolayer WSe_2 is the second-order Raman mode due to LA phonons at the M point in the Brillouin zone, which is labeled as 2LA(M).[40,41] Moreover, the highlighted peak of B^1_{2g} at ≈309 cm^{-1} shown in bilayer WSe_2 was absent in monolayer crystals, which was consistently observed for multilayer crystals of WSe_2.[42,43] The PL spectra shown in Fig. 1c revealed a relatively weak PL peak for the bilayer WSe_2 at 784.0 nm as compared with the monolayer WSe_2. On the basis of the Raman and PL results we confirm that controlled growth of bilayer WSe_2 domains was successfully performed on sapphire substrates.

SHG can serve as one reliable and nondestructive characterization method to identify the stacking orders of the atomically thin layers. As 2H stacked WSe_2 possesses centrosymmetry, inducing no SHG output. Meanwhile, the monolayer WSe_2 and 3R stacked WSe_2 show strong SHG output due to the break of centrosymmetry.[44] Fig. 1d and e show the optical image and the corresponding SHG intensity mapping for a WSe_2 crystal composed of both monolayer and bilayer domains. Compared to the strong SHG intensity of the monolayer WSe_2, no SHG signal can be detected for the bilayer region. In addition, a sharp boundary was observed crossing the two domains, which was consistent with the bilayer profile. As a result, the monolayer WSe_2 showed an obviously strong SHG response due to the lack of inversion symmetry, and meanwhile the bilayer WSe_2 was endowed with a typical 2H stacking order.

We have also performed additional SHG measurements for bilayer WSe_2 with diverse morphologies. As shown in Fig. S4 (ESI†), both bilayer crystals primarily exhibited 2H stacking, which has been further exemplified by the low-frequency Raman results shown in Fig. S5 (ESI†). It has been previously shown that the Raman bands in the high-frequency range are not sensitive to the change of interlayer van der Waals (vdW) interactions caused by different stacking configurations.[36,45] Distinct behaviors are found in ultra-low-frequency (ULF) Raman modes, in which the two peaks for 3R(2H) stacking bilayer WSe_2 belong to the in-plane shear mode (SM) and out-of-plane layer-breathing mode (LBM), respectively.[36] Therefore, the peak intensity ratio between LBM and SM can be used as an index to identify the stacking order of the bilayer WSe_2 complementary to SHG data. From Fig. S5 (ESI†), a clear decrease in the peak intensity of the SM from 2H to 3R stacking is observed with a corresponding increment in the LBM. Thus, the ULF Raman spectra of the various bilayer WSe_2 stacking configurations are in agreement with previous reports[36] and SHG data (Fig. S4, ESI†). For example, we note that the occasionally found irregular-shaped bilayer WSe_2 crystal showed 2H/3R mixed stacking configurations (Fig. S5b, ESI†), which is consistent with their corresponding SHG results shown in Fig. S4a (ESI†). Additionally, the stacking configurations can be studied with atomic precision using aberration-corrected STEM. The low-magnification HAADF-STEM

image of the top-view bilayer WSe_2 sample and corresponding elemental mapping images are shown in Fig. S6 (ESI†). In the *Z*-contrast high-angle-annular dark-field STEM imaging shown in Fig. 1f, the intensity strongly depends on the atomic weight and the number of monolayers. The high intensity sites correspond to the heavy atoms (*i.e.* W) or thicker sample, showing a contrast difference with the lighter Se atom. The STEM image clearly shows the arrangements of 2H stacked bilayer WSe_2,[36] corroborating the concluded results from SHG and low-frequency Raman.

In this work, we used as-supplied sapphire substrates to grow WSe_2 bilayer crystals for the investigation of the growth mechanism. For the CVD parameters grown on this type of substrate, both monolayer and bilayer WSe_2 crystals are inclined to be formed at random orientations, as shown in Fig. 1a. AFM measurements were further performed to study the growth mechanism of bilayer WSe_2 crystals. A few selected flakes yet to complete the bilayer growth were examined to explore the details. In Fig. 2a, the corresponding inset height profile yields the thickness of the WSe_2 crystal of ≈ 0.8 nm, in agreement with the previously reported thickness of monolayer WSe_2 crystals.[3] The small particles were the multilayer seeds occasionally observed in monolayer crystals.[46] From the zoomed-in image as shown in Fig. 2b, it's been found that the bilayer nuclei initially grow from the sapphire atomic steps (so-called "step direction"). This phenomenon was further demonstrated by a monolayer WSe_2 grain boundary crystal with bilayer nuclei on top, as shown in Fig. S7a and b (ESI†). The bilayer nuclei can be clearly seen initially growing along the sapphire atomic steps. These results provide a powerful argument with the fact that the bilayer nuclei growth originates from the atomic steps.

To better understand the influence of the atomic steps on the aligned growth of bilayer WSe_2 nuclei, we compared the step height and roughness of the area with and without being covered by WSe_2 monolayer and bilayer. Fig. 2c and d show representative AFM topographic images of the bilayer WSe_2 crystal. Interestingly, the corrugation features are evident from the bare sapphire surface shown in Fig. 2d and the corresponding height profile in Fig. 2e (right part; corrugations of 0.2 to 0.5 nm). In contrast, the pronounced atomic steps with a periodically distributed pattern can be seen on the location covered with monolayer as well as bilayer WSe_2 crystals. The periodicity and oscillation of the step heights also appear to be more regular than for the bare sapphire. These drastic atomic step heights are thought to be formed through strong interactions between WSe_2 and the sapphire terrace. The most striking observation was that the average atomic step height

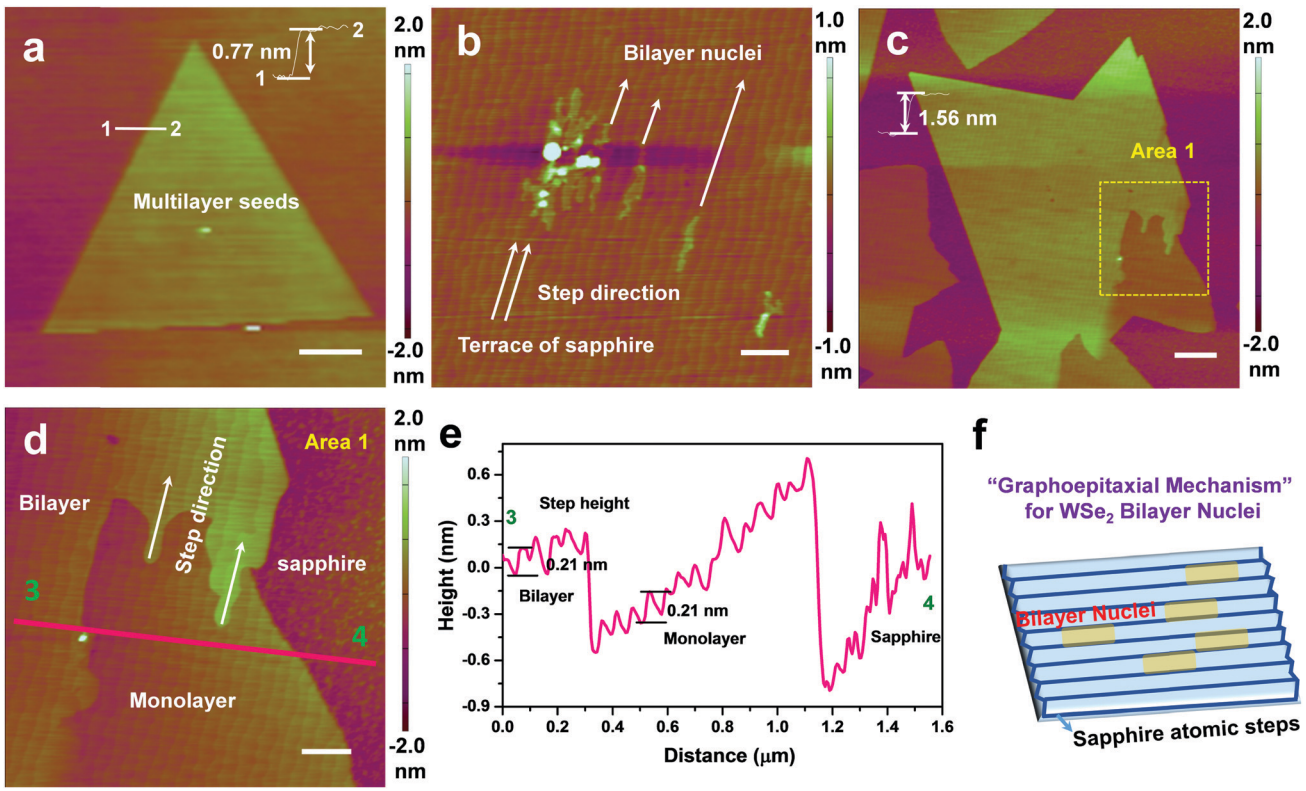

Fig. 2 (a and b) AFM topographic images of a monolayer WSe_2 crystal with bilayer nuclei in the center area. The inset height profile was ~0.8 nm, indicating a monolayer thickness of WSe_2. The zoomed-in AFM image in b shows initial WSe_2 bilayer nuclei aligned growth on the atomic steps of sapphire. (c and d) AFM topographic images of bilayer WSe_2 crystals. The inset height profile in c was ~1.6 nm, indicating a bilayer thickness of WSe_2. (e) The vertical profile was taken along the magenta line indicated in d (from 3 to 4). The average step height of sapphire terrace with monolayer/bilayer WSe_2 covering was ~0.2 nm. The small corrugation on the bare sapphire surface was 0.2–0.5 nm. (f) The proposed schematic of WSe_2 bilayer nuclei growth along the surface step nanogrooves of sapphire. The bilayer nuclei alignments on the atomic steps abide by the graphoepitaxial mechanism. Scale bars: a, 2 μm; b, 200 nm; c, 500 nm; d, 200 nm.

was ~0.21 nm for the sapphire with the WSe_2 grown on top. The height was similar to the step height measured on as-supplied sapphire after high temperature annealing (Fig. S8, ESI†) and the reported literature.[22,29,30]

Since the bilayer WSe_2 nuclei growth appears to be mediated by the atomic steps on sapphire's surface, we hypothesized that the bilayer WSe_2 nuclei alignment on the atomic steps could resemble the graphoepitaxy effect (see Fig. 2f). Such phenomenon is known to affect the crystallographic orientation of the overlayer in artificial surface-relief structures.[33,47,48] Two main factors are proposed to be involved in the graphoepitaxy mechanism of bilayer nuclei aligned growth: Firstly, we find that the atomic steps with the WSe_2 layer atop have become more vivid (see relevant AFM analysis) as compared with the bare sapphire, which is similar to the phenomena obtained by different artificial means,[47,48] and high-temperature annealing.[22,29,30,49] Secondly, the pronounced atomic steps could enhance the seeding of the bilayer nuclei owing to energy lowering and thus lead to the bilayer nuclei growth orientation following the step direction.

In addition, once the monolayer/bilayer WSe_2 nucleates on the sapphire, the surface adsorbates were driven out and the surface roughness reduces (Fig. S9 and Table S1, ESI†). We attribute this to the fact that the irregularly small corrugations seen on the bare sapphire are glossed over by the WSe_2 crystals, *i.e.* being smoothened out. A similar reduction in surface roughness is observed on the bare sapphire surface upon annealing at high temperatures (see Table S1, ESI†). Hence, the pronounced atomic step heights and the ultrasmooth surface induced by the WSe_2 crystal atop are proposed as the main reasons for the bilayer nuclei initially growing on the atomic steps of sapphire. Moreover, the same growth mode also applies to the 3rd layer WSe_2. Fig. 3a and b illustrate the typical bilayer WSe_2 with the 3rd layer WSe_2 nuclei growing along the atomic steps of sapphires. The Raman spectra for the trilayer WSe_2 are shown in Fig. S10 (ESI†). Fig. S11 (ESI†) shows more examples validating the bilayer nuclei growth behaviors. Taking the bilayer WSe_2 growth as an example, we illustrate in Fig. 3e with schematics how the bilayer WSe_2 nuclei nucleate along the enhanced atomic steps (yellow solid lines) and eventually become a superimposed bilayer crystal, following a layer-by-layer (LBL) growth mode.[50,51] Although the growth orientation of the upper layer nuclei was guided by the sapphire substrate steps, the stacking configuration of the upper layer seems irrelevant to the underlying sapphire crystal orientation. The first layer WSe_2 are not oriented in the same direction but the upper layers could still recognize the crystal lattice of the first layer WSe_2 to form 2H stacking configurations, suggesting that the second layer crystal stacking is governed by the vdW epitaxial processes on the first layer of WSe_2.

Charge transport measurements were performed to evaluate the electronic property of our bilayer WSe_2 crystals as-grown on sapphire substrates. Standard electron beam lithography was used to fabricate side-gate bilayer WSe_2 field-effect transistors directly on sapphire substrates. Device structure and a representative optical image of the device are shown in Fig. 4a, where Pd (20 nm)/Au (70 nm) was used as the contact metal and an ionic liquid (C_g = 5.0 μF cm^{-2}) was dropped across the channel as the top gate dielectric material. The Raman and PL of the

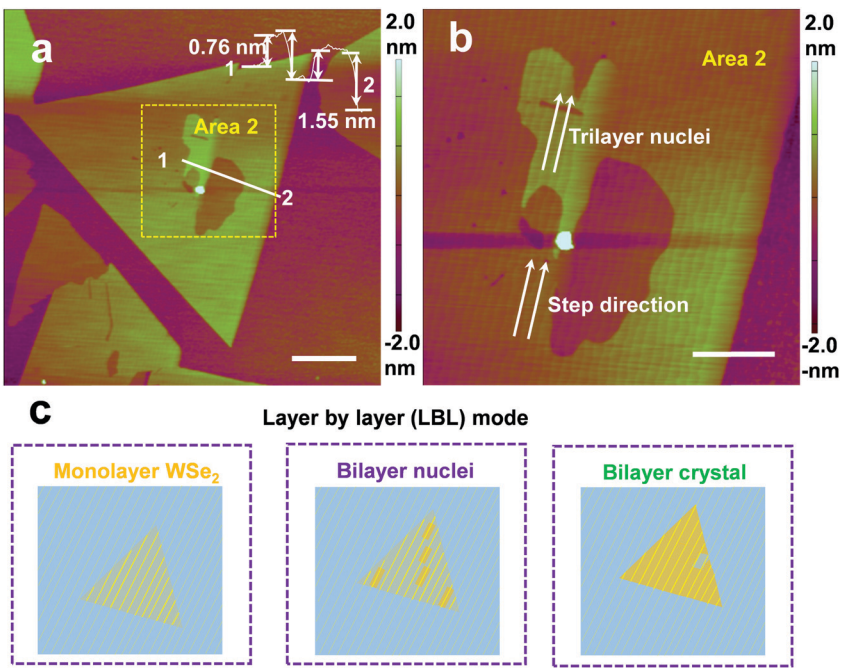

Fig. 3 (a) AFM topographic images of a bilayer WSe_2 crystal with the 3rd layer nuclei. The inset height profile demonstrated a bilayer thickness of WSe_2 and trilayer nuclei formed on the topmost surface. (b) The zoomed-in AFM image in a showed WSe_2 bilayer and trilayer nuclei growth guided by the atomic steps. (c) Schematics of the layer-by-layer growth mode in this work. The yellow dashed lines are the atomic steps of the bare sapphire and the yellow solid lines are the atomic steps of sapphire with WSe_2 crystals atop. Scale bars: a, 1 μm; b, 500 nm.

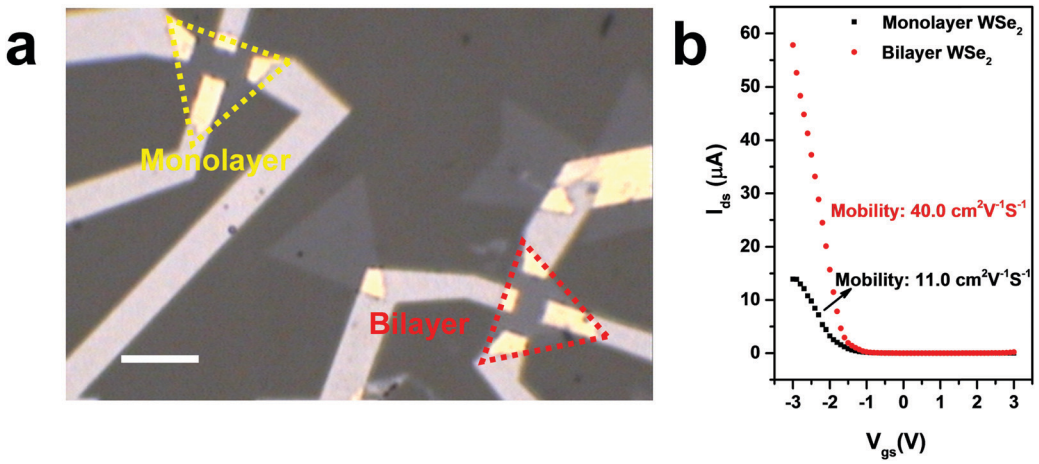

Fig. 4 (a) Optical image of monolayer/bilayer WSe_2 crystals for the device fabrication. Scale bar: 15 μm; (b) I_{ds} as a function of V_{gs} for monolayer/bilayer WSe_2 crystals device. V_d = 0.5 V, C_g = 5.0 μF cm^{-2}. The mobility of monolayer and bilayer crystals were measured to be 11.0 and 40.0 cm^2 V^{-1} s^{-1}, respectively.

WSe_2 samples before and after fabrication are shown in Fig. S12 (ESI†) to confirm the quality of the samples. Unfortunately, the quality of the WSe_2 samples appears to be compromised after device fabrication probably due to PMMA contamination during the EBL process. Device characterization was carried out in a vacuum chamber at room temperature to exclude unwanted doping effects due to H_2O or O_2 present in ambient air. The voltage applied between the source and drain electrodes (V_D) was varied from −2 to 2 V for both monolayer and bilayer crystal-based devices, as shown in Fig. S13a and b (ESI†), indicating the good contact of the metal with the WSe_2 channel. Both devices exhibit predominantly p-channel characteristics in accordance with previously published results, but with evidence of pronounced electron transport under positive V_G. Interestingly, monolayer WSe_2-based transistors appear to be more ambipolar than bilayer WSe_2 devices. The hole mobility extracted from the transfer characteristics in Fig. 4b were ≈11 cm^2 V^{-1} s^{-1} and ≈40 cm^2 V^{-1} s^{-1} for monolayer and bilayer WSe_2 crystals, respectively. Moreover, the subthreshold slopes (SS) for monolayer and bilayer WSe_2 transistors were 229 mV dec^{-1} and 201 mV dec^{-1}, respectively, as shown in Fig. S13c (ESI†). The similarity in the derived SS values indicates good gate control over the p-channel for both monolayer and bilayer WSe_2 FETs.

It has been reported that the hole mobility in monolayer and multilayer TMD devices is affected by intrinsic phonon scattering within the channel as well as extrinsic scattering phenomena originating from charged impurities at the channel/dielectric interface, charge trapping states, substrate surface roughness and remote surface optical phonons.[52–54] In particular, coulomb scattering from charged impurities at the channel/substrate interface has been proposed as the primary reason for the lower room-temperature mobility in TMDs.[52–54] Meanwhile, the intrinsic mobility of bilayer TMD is also predicted to be higher than monolayer TMD.[55] Overall, the field-effect measurements suggest that our CVD bilayer WSe_2 crystals are of good quality and thus hold promising prospects toward applications in nanoelectronic devices.

Conclusions

In conclusion, we have demonstrated controlled growth of 2H stacked bilayer WSe_2 on *c*-plane sapphire substrates by the CVD method. The pure 2H stacking configuration of bilayer WSe_2 was confirmed by collective characterization techniques including SHG, low-frequency Raman and STEM measurements. We demonstrate the nuclei growth of bilayer WSe_2 sliding along the pronounced atomic steps induced by WSe_2 crystals atop, resembling the graphoepitaxy mechanism. And the alignment growth of bilayer nuclei on atomic steps gives rise to the gradual formation of overlapped bilayer crystals, abiding by the LBL growth mode. Importantly, the bilayers in our growth conditions lead to the most thermodynamically stable 2H stacked bilayer WSe_2 through vdW epitaxial growth, exhibiting substantially enhanced hole mobility, three times higher than that of monolayer WSe_2. The discovery of atomic steps guiding bilayer nuclei growth revealed in this work provides new insights into the growth, which could be applicable to other TMD systems, hence paving the way towards controllable large-area growth of bilayer and multilayer TMDs crystals for electronic and optoelectronic applications.

Methods

Material synthesis

The monolayer/bilayer WSe_2 crystals were grown by the chemical vapor deposition (CVD) method. Typically, WO_3 powder (300 mg, Sigma-Aldrich, 99.9%) was placed into a quartz boat in a high temperature furnace, while the Se powder (Sigma-Aldrich, 99.99%) was placed into a separate low temperature furnace upstream of WO_3. The carrier gas of H_2 and Ar allows the diffusion of Se vapor into the reaction area. During the heating stage, H_2 firstly reacts with WO_3 to form WO_{3-x} (x = 0–3) suboxides. With regard to the WSe_2 growth stage, all WSe_2 formation reactions were equally given 15 min growth time starting at 0 min when the temperature of the WO_3 furnace reached 890–900 °C. The Se powder in the low temperature zone was heated to 250–260 °C and carried

downstream using the carrier gas to the reaction area at times of 3 min before the WO_3 precursors reached the required temperature. The *c*-plane sapphire substrates were put downstream of the WO_3 boat, where the Se and WO_3 vapors were brought to the sapphire substrates by the carrier gas. The sapphire substrates are directly used without any pre-treatment. Finally, the furnace was naturally cooled down to room temperature after the temperature controller was turned off.

Raman and AFM characterization

The as-grown WSe_2 crystals are characterized using optical microscopy (Witec alpha 300 confocal Raman microscope) equipped with a confocal spectrometer using a 532 nm excitation laser. A typical laser spot is 1–2 μm. The thickness of the WSe_2 crystals was determined by atomic force microscope (AFM, Cypher ES model from Asylum Research Oxford Instruments).

SHG characterization

The SHG measurements were carried out using a Horiba Jobin–Yvon HR800 spectrometer in reflection geometry with the excitation laser perpendicular to the substrate. A mode-locked Ti/Sapphire oscillator was used as the pumping source at 800 nm wavelength (Spectra-Physics, 80 MHz, 100 fs). With a 100× objective, the pumping light was focused to a spot size of ~2 μm in diameter on the sample. For measurement of SHG intensity mapping, the excitation laser was modulated under DuoScan mode, which is a unique hardware module to scan the laser beam on a given area using software controlled mirrors.

STEM sample preparation and characterization

The WSe_2 crystals were coated with polymethylmethacrylate (PMMA) to support the film during the transfer process. To separate the film from the sapphire substrate, the samples were soaked in an HF solution ($HF:H_2O = 1:1$) for 15 min. After rinsing with deionized water several times, the samples were dipped into water and the film was released from the substrate by tweezers. With the film floating on the water surface, we used a QUANTIFOIL holey carbon film on a 400 Mesh Nickel TEM grid (Agar Scientific) to scoop the film. The PMMA was then removed by acetone for more than 1 h. The TEM grid with WSe_2 crystals was finally baked in a vacuum ($<10^{-6}$ Torr) at 350 °C overnight to remove the PMMA residue. HAADF-STEM imaging was conducted at 80 kV using a ThermoFisher USA (former FEI Co) Titan Themis Z (40–300 kV) TEM equipped with a double Cs (spherical aberration) corrector, a high brightness electron gun (x-FEG) and a Fischione STEM detector.

Device fabrication and transport measurement

FETs were fabricated on WSe_2 monolayer and bilayer crystals directly on sapphire substrates under the same conditions. The devices were fabricated by the standard E-beam lithography (EBL) process using a PMMA 950 A4 photoresist. Before the exposure, a thick sputtered Au film (6 nm in thickness) was coated on the photoresist to avoid the severe charging effect on the sapphire surface. The first EBL process was to make the alignment markers on the sapphire surface and the second process was to pattern the source-drain and gate electrodes, followed by e-beam evaporation of Pd (20 nm)/Au (70 nm) and a standard lift-off process by acetone. The FET transfer characteristics were measured under vacuum by a Keithley 4200 semiconductor parameter analyzer (V_d = 0.5 V). The ionic liquid (C_g = 5.0 μF cm^{-2}) was used to gate WSe_2 and the p-type semiconductor behavior.

Author contributions

The manuscript was written through contributions of all authors. All authors have given approval to the final version of the manuscript.

Conflicts of interest

There are no conflicts to declare.

Acknowledgements

T. D. A., V. T., X. Z., and L. L. acknowledge the support from King Abdullah University of Science and Technology. V. T. acknowledges the support from User Proposals (#4420 and #5067) at the Molecular Foundry, Lawrence Berkeley National Lab, supported by the Office of Basic Energy Sciences, of the U.S. Department of Energy under Contract No. DE-AC02-05CH11231. We would also like to acknowledge the support from Core Lab in KAUST.

References

1 M.-Y. Li, S.-K. Su, H.-S. P. Wong and L.-J. Li, How 2D semiconductors could extend Moore's law, *Nature*, 2019, **567**, 169.
2 C. Huang, S. Wu, A. M. Sanchez, J. J. P. Peters, R. Beanland, J. S. Ross, P. Rivera, W. Yao, D. H. Cobden and X. Xu, Lateral heterojunctions within monolayer $MoSe_2$–WSe_2 semiconductors, *Nat. Mater.*, 2014, **13**, 1096.
3 M.-Y. Li, Y. Shi, C.-C. Cheng, L.-S. Lu, Y.-C. Lin, H.-L. Tang, M.-L. Tsai, C.-W. Chu, K.-H. Wei, J.-H. He, W.-H. Chang, K. Suenaga and L.-J. Li, Epitaxial growth of a monolayer WSe_2-MoS_2 lateral p-n junction with an atomically sharp interface, *Science*, 2015, **349**(6247), 524–528.
4 A.-Y. Lu, H. Zhu, J. Xiao, C.-P. Chuu, Y. Han, M.-H. Chiu, C.-C. Cheng, C.-W. Yang, K.-H. Wei, Y. Yang, Y. Wang, D. Sokaras, D. Nordlund, P. Yang, D. A. Muller, M.-Y. Chou, X. Zhang and L.-J. Li, Janus monolayers of transition metal dichalcogenides, *Nat. Nanotechnol.*, 2017, **12**, 744.
5 A. Pospischil, M. M. Furchi and T. Mueller, Solar-energy conversion and light emission in an atomic monolayer p–n diode, *Nat. Nanotechnol.*, 2014, **9**, 257.
6 Q. H. Wang, K. Kalantar-Zadeh, A. Kis, J. N. Coleman and M. S. Strano, Electronics and optoelectronics of two-dimensional transition metal dichalcogenides, *Nat. Nanotechnol.*, 2012, **7**, 699.
7 C.-H. Lee, G.-H. Lee, A. M. van der Zande, W. Chen, Y. Li, M. Han, X. Cui, G. Arefe, C. Nuckolls, T. F. Heinz, J. Guo,

J. Hone and P. Kim, Atomically thin p–n junctions with van der Waals heterointerfaces, *Nat. Nanotechnol.*, 2014, **9**, 676.

8 V. Nicolosi, M. Chhowalla, M. G. Kanatzidis, M. S. Strano and J. N. Coleman, Liquid Exfoliation of Layered, *Mater. Sci.*, 2013, **340**, 6139.

9 J. Zhou, J. Lin, X. Huang, Y. Zhou, Y. Chen, J. Xia, H. Wang, Y. Xie, H. Yu, J. Lei, D. Wu, F. Liu, Q. Fu, Q. Zeng, C.-H. Hsu, C. Yang, L. Lu, T. Yu, Z. Shen, H. Lin, B. I. Yakobson, Q. Liu, K. Suenaga, G. Liu and Z. Liu, A library of atomically thin metal chalcogenides, *Nature*, 2018, **556**(7701), 355–359.

10 Q. Feng, N. Mao, J. Wu, H. Xu, C. Wang, J. Zhang and L. Xie, Growth of $MoS_{2(1-x)}Se_{2x(x\ =\ 0.41\text{–}1.00)}$ Monolayer Alloys with Controlled Morphology by Physical Vapor Deposition, *ACS Nano*, 2015, **9**(7), 7450–7455.

11 C. Gong, C. Huang, J. Miller, L. Cheng, Y. Hao, D. Cobden, J. Kim, R. S. Ruoff, R. M. Wallace, K. Cho, X. Xu and Y. J. Chabal, Metal Contacts on Physical Vapor Deposited Monolayer MoS_2, *ACS Nano*, 2013, **7**(12), 11350–11357.

12 J.-H. Huang, K.-Y. Deng, P.-S. Liu, C.-T. Wu, C.-T. Chou, W.-H. Chang, Y.-J. Lee and T.-H. Hou, Large-Area 2D Layered $MoTe_2$ by Physical Vapor Deposition and Solid-Phase Crystallization in a Tellurium-Free Atmosphere, *Adv. Mater. Interfaces*, 2017, **4**(17), 1700157.

13 H. J. Liu, L. Jiao, L. Xie, F. Yang, J. L. Chen, W. K. Ho, C. L. Gao, J. F. Jia, X. D. Cui and M. H. Xie, Molecular-beam epitaxy of monolayer and bilayer WSe_2: a scanning tunneling microscopy/spectroscopy study and deduction of exciton binding energy, *2D Mater.*, 2015, **2**(3), 034004.

14 A. Roy, H. C. P. Movva, B. Satpati, K. Kim, R. Dey, A. Rai, T. Pramanik, S. Guchhait, E. Tutuc and S. K. Banerjee, Structural and Electrical Properties of $MoTe_2$ and $MoSe_2$ Grown by Molecular Beam Epitaxy, *ACS Appl. Mater. Interfaces*, 2016, **8**(11), 7396–7402.

15 K. F. Mak, K. He, J. Shan and T. F. Heinz, Control of valley polarization in monolayer MoS_2 by optical helicity, *Nat. Nanotechnol.*, 2012, **7**, 494.

16 H. Zeng, J. Dai, W. Yao, D. Xiao and X. Cui, Valley polarization in MoS_2 monolayers by optical pumping, *Nat. Nanotechnol.*, 2012, **7**, 490.

17 F. Withers, O. Del Pozo-Zamudio, A. Mishchenko, A. P. Rooney, A. Gholinia, K. Watanabe, T. Taniguchi, S. J. Haigh, A. K. Geim, A. I. Tartakovskii and K. S. Novoselov, Light-emitting diodes by band-structure engineering in van der Waals heterostructures, *Nat. Mater.*, 2015, **14**, 301.

18 K. F. Mak and J. Shan, Photonics and optoelectronics of 2D semiconductor transition metal dichalcogenides, *Nat. Photonics*, 2016, **10**, 216.

19 J. R. Schaibley, H. Yu, G. Clark, P. Rivera, J. S. Ross, K. L. Seyler, W. Yao and X. Xu, Valleytronics in 2D materials, *Nat. Rev. Mater.*, 2016, **1**, 16055.

20 J. Chen, B. Liu, Y. Liu, W. Tang, C. T. Nai, L. Li, J. Zheng, L. Gao, Y. Zheng, H. S. Shin, H. Y. Jeong and K. P. Loh, Chemical Vapor Deposition of Large-Sized Hexagonal WSe_2 Crystals on Dielectric Substrates, *Adv. Mater.*, 2015, **27**(42), 6722–6727.

21 L. Chen, B. Liu, A. N. Abbas, Y. Ma, X. Fang, Y. Liu and C. Zhou, Screw-Dislocation-Driven Growth of Two-Dimensional Few-Layer and Pyramid-like WSe_2 by Sulfur-Assisted Chemical Vapor Deposition, *ACS Nano*, 2014, **8**(11), 11543–11551.

22 L. Chen, B. Liu, M. Ge, Y. Ma, A. N. Abbas and C. Zhou, Step-Edge-Guided Nucleation and Growth of Aligned WSe_2 on Sapphire via a Layer-over-Layer Growth Mode, *ACS Nano*, 2015, **9**(8), 8368–8375.

23 J. Liu, M. Zeng, L. Wang, Y. Chen, Z. Xing, T. Zhang, Z. Liu, J. Zuo, F. Nan, R. G. Mendes, S. Chen, F. Ren, Q. Wang, M. H. Rümmeli and L. Fu, Ultrafast Self-Limited Growth of Strictly Monolayer WSe_2 Crystals, *Small*, 2016, **12**(41), 5741–5749.

24 M. Xia, B. Li, K. Yin, G. Capellini, G. Niu, Y. Gong, W. Zhou, P. M. Ajayan and Y.-H. Xie, Spectroscopic Signatures of AA′ and AB Stacking of Chemical Vapor Deposited Bilayer MoS2, *ACS Nano*, 2015, **9**(12), 12246–12254.

25 A. Zobel, A. Boson, P. M. Wilson, D. S. Muratov, D. V. Kuznetsov and A. Sinitskii, Chemical vapour deposition and characterization of uniform bilayer and trilayer MoS_2 crystals, *J. Mater. Chem. C*, 2016, **4**(47), 11081–11087.

26 S. Yang, J. Kang, Q. Yue and K. Yao, Vapor Phase Growth and Imaging Stacking Order of Bilayer Molybdenum Disulfide, *J. Phys. Chem. C*, 2014, **118**(17), 9203–9208.

27 H. Ye, J. Zhou, D. Er, C. C. Price, Z. Yu, Y. Liu, J. Lowengrub, J. Lou, Z. Liu and V. B. Shenoy, Toward a Mechanistic Understanding of Vertical Growth of van der Waals Stacked 2D Materials: A Multiscale Model and Experiments, *ACS Nano*, 2017, **11**(12), 12780–12788.

28 S. Ghatak, A. N. Pal and A. Ghosh, Nature of Electronic States in Atomically Thin MoS_2 Field-Effect Transistors, *ACS Nano*, 2011, **5**(10), 7707–7712.

29 M. Yoshimoto, T. Maeda, T. Ohnishi, H. Koinuma, O. Ishiyama, M. Shinohara, M. Kubo, R. Miura and A. Miyamoto, Atomic-scale formation of ultrasmooth surfaces on sapphire substrates for high-quality thin-film fabrication, *Appl. Phys. Lett.*, 1995, **67**(18), 2615–2617.

30 D. Dumcenco, D. Ovchinnikov, K. Marinov, P. Lazić, M. Gibertini, N. Marzari, O. L. Sanchez, Y.-C. Kung, D. Krasnozhon, M.-W. Chen, S. Bertolazzi, P. Gillet, A. Fontcuberta i Morral, A. Radenovic and A. Kis, Large-Area Epitaxial Monolayer MoS_2, *ACS Nano*, 2015, **9**(4), 4611–4620.

31 S. Han, X. Liu and C. Zhou, Template-Free Directional Growth of Single-Walled Carbon Nanotubes on a- and r-Plane Sapphire, *J. Am. Chem. Soc.*, 2005, **127**(15), 5294–5295.

32 A. Ismach, L. Segev, E. Wachtel and E. Joselevich, Atomic-Step-Templated Formation of Single Wall Carbon Nanotube Patterns, *Angew. Chem., Int. Ed.*, 2004, **43**(45), 6140–6143.

33 D. Tsivion, M. Schvartzman, R. Popovitz-Biro, P. von Huth and E. Joselevich, Guided Growth of Millimeter-Long Horizontal Nanowires with Controlled Orientations, *Science*, 2011, **333**(6045), 1003–1007.

34 S. Saadi, F. Abild-Pedersen, S. Helveg, J. Sehested, B. Hinnemann, C. C. Appel and J. K. Nørskov, On the Role of Metal Step-Edges in Graphene Growth, *J. Phys. Chem. C*, 2010, **114**(25), 11221–11227.

35 S. Curiotto and D. Chatain, Surface composition and morphology of c-, and m-sapphire surfaces in O_2 and H_2 environments, *Surf. Sci.*, 2009, **603**(17), 2688–2697.

36 A. A. Puretzky, L. Liang, X. Li, K. Xiao, K. Wang, M. Mahjouri-Samani, L. Basile, J. C. Idrobo, B. G. Sumpter, V. Meunier and D. B. Geohegan, Low-Frequency Raman Fingerprints of Two-Dimensional Metal Dichalcogenide Layer Stacking Configurations, *ACS Nano*, 2015, **9**(6), 6333–6342.

37 J. He, K. Hummer and C. Franchini, Stacking effects on the electronic and optical properties of bilayer transition metal dichalcogenides, *Phys. Rev. B: Condens. Matter Mater. Phys.*, 2014, **89**(7), 075409.

38 J.-K. Huang, J. Pu, C.-L. Hsu, M.-H. Chiu, Z.-Y. Juang, Y.-H. Chang, W.-H. Chang, Y. Iwasa, T. Takenobu and L.-J. Li, Large-Area Synthesis of Highly Crystalline WSe_2 Monolayers and Device Applications, *ACS Nano*, 2014, **8**(1), 923–930.

39 H. Kim, S. J. Yun, J. C. Park, M. H. Park, J.-H. Park, K. K. Kim and Y. H. Lee, Seed Growth of Tungsten Diselenide Nanotubes from Tungsten Oxides, *Small*, 2015, **11**(18), 2192–2199.

40 A. Molina-Sánchez and L. Wirtz, Phonons in single-layer and few-layer MoS_2 and WS_2, *Phys. Rev. B: Condens. Matter Mater. Phys.*, 2011, **84**(15), 155413.

41 C. Sourisseau, F. Cruege, M. Fouassier and M. Alba, Second-order Raman effects, inelastic neutron scattering and lattice dynamics in 2H-WS_2, *Chem. Phys.*, 1991, **150**(2), 281–293.

42 W. Zhao, Z. Ghorannevis, K. K. Amara, J. R. Pang, M. Toh, X. Zhang, C. Kloc, P. H. Tan and G. Eda, Lattice dynamics in mono- and few-layer sheets of WS_2 and WSe_2, *Nanoscale*, 2013, **5**(20), 9677–9683.

43 Y. Zhao, X. Luo, H. Li, J. Zhang, P. T. Araujo, C. K. Gan, J. Wu, H. Zhang, S. Y. Quek, M. S. Dresselhaus and Q. Xiong, Interlayer Breathing and Shear Modes in Few-Trilayer MoS_2 and WSe_2, *Nano Lett.*, 2013, **13**(3), 1007–1015.

44 W.-T. Hsu, Z.-A. Zhao, L.-J. Li, C.-H. Chen, M.-H. Chiu, P.-S. Chang, Y.-C. Chou and W.-H. Chang, Second Harmonic Generation from Artificially Stacked Transition Metal Dichalcogenide Twisted Bilayers, *ACS Nano*, 2014, **8**(3), 2951–2958.

45 J. Xia, J. Yan and Z. X. Shen, Transition metal dichalcogenides: structural, optical and electronic property tuning *via* thickness and stacking, *FlatChem*, 2017, **4**, 1–19.

46 A. Aljarb, Z. Cao, H.-L. Tang, J.-K. Huang, M. Li, W. Hu, L. Cavallo and L.-J. Li, Substrate Lattice-Guided Seed Formation Controls the Orientation of 2D Transition-Metal Dichalcogenides, *ACS Nano*, 2017, **11**(9), 9215–9222.

47 M. W. Geis, D. C. Flanders and H. I. Smith, Crystallographic orientation of silicon on an amorphous substrate using an artificial surface-relief grating and laser crystallization, *Appl. Phys. Lett.*, 1979, **35**(1), 71–74.

48 M. W. Geis, B. Y. Tsaur and D. C. Flanders, Graphoepitaxy of germanium on gratings with square-wave and sawtooth profiles, *Appl. Phys. Lett.*, 1982, **41**(6), 526–529.

49 C. Barth and M. Reichling, Imaging the atomic arrangements on the high-temperature reconstructed α-Al_2O_3(0001) surface, *Nature*, 2001, **414**, 54.

50 M. Kawasaki, K. Takahashi, T. Maeda, R. Tsuchiya, M. Shinohara, O. Ishiyama, T. Yonezawa, M. Yoshimoto and H. Koinuma, Atomic Control of the $SrTiO_3$ Crystal, *Surf. Sci.*, 1994, **266**(5190), 1540–1542.

51 K. Yan, H. Peng, Y. Zhou, H. Li and Z. Liu, Formation of Bilayer Bernal Graphene: Layer-by-Layer Epitaxy *via* Chemical Vapor Deposition, *Nano Lett.*, 2011, **11**(3), 1106–1110.

52 B. Radisavljevic and A. Kis, Mobility engineering and a metal–insulator transition in monolayer MoS_2, *Nat. Mater.*, 2013, **12**, 815.

53 K. Kaasbjerg, K. S. Thygesen and K. W. Jacobsen, Phonon-limited mobility in n-type single-layer MoS_2 from first principles, *Phys. Rev. B: Condens. Matter Mater. Phys.*, 2012, **85**(11), 115317.

54 W. Liu, J. Kang, D. Sarkar, Y. Khatami, D. Jena and K. Banerjee, Role of Metal Contacts in Designing High-Performance Monolayer n-Type WSe_2 Field Effect Transistors, *Nano Lett.*, 2013, **13**(5), 1983–1990.

55 B. W. H. Baugher, H. O. H. Churchill, Y. Yang and P. Jarillo-Herrero, Intrinsic Electronic Transport Properties of High-Quality Monolayer and Bilayer MoS_2, *Nano Lett.*, 2013, **13**(9), 4212–4216.

